Synthesis, structural, optical, and dielectric properties of CuWO$_4$/PVP/Cs bio-nanocomposites for some industrial applications

Adel M. El Sayed[1], M. I. A. Abdel Maksoud[2,*] , Said M. Kassem[2], and A. S. Awed[3]

[1] *Physics Department, Faculty of Science, Fayoum University, El-Fayoum 63514, Egypt*

[2] *National Center for Radiation Research and Technology (NCRRT), Egyptian Atomic Energy Authority (EAEA), Nasr City, Cairo, Egypt*

[3] *Higher Institute for Engineering and Technology at Manzala, El Manzala, Egypt*

ABSTRACT

The nanocomposites of biopolymers and bimetallic oxides are exciting classes of materials. Besides the economic and environmental considerations, these materials became the best candidates for various applications in industry and medicine. In this study, CuWO$_4$ nanoparticles (NP) with high purity were prepared by co-precipitation and loaded into poly(vinyl pyrrolidone)/chitosan (PVP/Cs) films. XRD results showed that CuWO$_4$ has a triclinic phase with an average crystallite size of 43 nm. PVP/Cs is semi-crystalline blend and its crystallinity degraded by CuWO$_4$ incorporation. EDX analysis was used to study the chemical composition of all samples. FE-SEM showed that CuWO$_4$ has particle sizes of 50–150 nm and that the crack-free surface of PVP/Cs became rougher and more porous after loading of CuWO$_4$ NP. FTIR confirmed the presence of the reactive functional group of CuWO$_4$, PVP, and Cs and that the low doping ratio of CuWO$_4$ NP restricted the functional group's vibrations. The UV–vis–NIR investigation showed that the films have a small absorption index and high transmittance in the range of 68–90%. The direct and indirect band gaps (E_g^{dir} and E_g^{ind}) of the blend were found equal to 5.0 and 4.2 eV and can be tuned by CuWO$_4$ content. Similarly, the index of refraction and carrier concentration/electron effective mass ratio (N/m*), the dielectric constant ($\varepsilon' = 8.3$–24.5), and the dielectric loss depend on the applied frequency, temperature, and CuWO$_4$ filler content. The conductivity (σ_{ac}) ranges from 1.2×10^{-6} to 9.16×10^{-4} S/m and exhibits the Arrhenius behavior. The optical and dielectric results show that the prepared PNC may suit some energy storage device,s such as supercapacitors, and organic optoelectronic devices, such as light emitting diodes and/or photovoltaic solar cells.

Address correspondence to E-mail: muhamadabdelmaksoud@gmail.com; muhamadmqsod@gmail.com

1 Introduction

In recent years, the development of nanocomposites based on biopolymers mixed with bimetallic oxides has attracted increasing attention. The predominant reason evoked for this trend is the lower cost and ease of polymer nanocomposites (PNC) preparation with properties that make them suitable candidates for potential applications in various fields of industry, such as environment-friendly electronics, food packaging, and medical and pharmaceutical applications [1–6].

Among the bimetallic oxides, the copper tungstates ($CuWO_4$) have attracted considerable attention as photoelectrode owing to its high redox, excellent chemical stability of the crystalline $CuWO_4$ in aqueous solutions, excellent catalytic performance, and the moderate band gap (E_g = 2.2–2.4 eV) which permits a theoretical photocurrent density up to 10.7 mA/cm^2 [7]. It exhibits a photoresponse with a cut-off wavelength of ~ 540 nm. Besides, the metal-to-metal ($Cu^{2+} \rightarrow W^{6+}$) charge transfer in $CuWO_4$ results in an absorption band at 850 nm. According to Chen et al. [8], the E_g value can be tuned by adjusting the elemental chemical composition $CuWO_4$, where an increase in Cu/W ratio from 0.33 to 2.5 decreases the E_g to 1.88 eV. Moreover, $CuWO_4$ is an n-type semiconductor, and the valence band (VB) and conduction band (CB) positions are positive (+ 2.6–2.7 V_{RHE} and + 0.4 V_{RHE}, respectively) on the normal hydrogen electrode scale, leading to the generation of photo-excited holes with strong oxidation ability [9]. The VB consists of strongly hybridized states of O 2p and Cu 3d, while the CB minimum comprises unoccupied Cu 3d states [7]. These properties make the material a candidate for novel functions in the fields of optics, fluorescence detection [10], photodegradation and water decomposition reactions, and fuel cell reactions. Currently, $CuWO_4$ has gained extensive interest in electrochemical sensors and supercapacitor applications [5, 11].

$CuWO_4$ in the form of nanopowder and films was prepared by several routes; Nong et al. [5] designed an electrochemical Chit-Au/$CuWO_4$@MoS_2 immunosensor that showed reproducibility, stability, and good repeatability for detecting cortisol. Lee et al. [7] fabricated $CuWO_4$ films on FTO substrates by the sol–gel method and spin-coating followed by thermal annealing for PEC water splitting. Serwar et al. [9] prepared $CuWO_4$ NP and $CuWO_4$/graphene QDs photocatalysts by co-precipitation and hydrothermal methods, respectively. Sun et al. [10] prepared $CuWO_4$ via the polyacrylamide gel method and obtained the pure triclinic phase after calcination of the xerogel at 900 °C. Du et al. [12] prepared MWO_4 (M = Co, Ni, Zn, and Cu) nanosheets on Ni foam by a hydrothermal method for efficient urea oxidation. Jatav et al. [13] fabricated AgI/$CuWO_4$ by a precipitation method for efficient visible-light photocatalysts for ciprofloxacin and RhB degradation.

One of the naturally occurring and abundant cationic polysaccharides is the chitosan (Cs) biopolymer. Cs obtained from chitin by alkaline N-acetylation via a thermochemical reaction. The low cost, high nitrogen content, biodegradability, hydrophilic properties, nontoxicity, reproducibility, good molecular biocompatibility, and antioxidant, antibacterial, and immunomodulatory properties make Cs a promising polymer for various biomedical, biotechnological, and green packaging applications, as well as for artificial skin, bone substitutes, agriculture, and cosmetics. Because of OH and NH_2 groups, Cs can exhibit interesting chelating and film-forming properties. The NH_2 serves as an electron donor, containing a lone pair electron. It serves the process of complexing and coordinating between the cations of loaded filler into the electrolyte membrane of batteries and acting as a sensor to detect glucose, catechol, and hazardous mercury [4, 14–18]. Moreover, Cs have a semi-crystalline nature and mixing them with another polymer may improve and widen the blend's multi-functionality. In this context, poly(vinyl pyrrolidone) (PVP) is an amorphous polymer and could improve the film-forming ability. In addition, PVP has a higher resistivity than Cs to ultraviolet rays. Therefore, adding PVP into Cs will maintain or improve the physicochemical properties and expand the Cs utilization to include the electrochemical applications, such as batteries and displays [19, 20].

Few reports on PNC based on $CuWO_4$ filler are found. Thiruppathi et al. [6] prepared $CuWO_4$/PMMA nanocomposite as a photocatalyst for some dyes and antibiotics. To the best of the authors' knowledge, this is the first attempt to explore the effect of $CuWO_4$ on the physicochemical properties of the PVP/Cs biopolymer blend. This report focuses on preparing $CuWO_4$ by the co-precipitation route and $CuWO_4$/PVP/Cs nanocomposites by solution casting. The morphological, structural, chemical composition, optical, and dielectric properties of the PVP/Cs biopolymer loaded with different filler ratios were investigated.

As mentioned above, we aim to enhance and expand the technological and medical applications of PVP/Cs bio-blend.

2 Experimental section

2.1 Preparation of CuWO$_4$ NPs

Sigma-Aldrich provided copper (II) chloride (CuCl$_2$) and sodium tungstate dihydrate (Na$_2$WO$_4$.2H$_2$O) as Cu and W sources. The co-precipitation method generated pure CuWO$_4$ NPs; the Cu and W salts were first dissolved in different beakers containing 400 mL of deionized water. Both of these solutions were mixed and magnetized strongly for 30 min. The CuWO$_4$ precipitate was centrifuged and washed three times with deionized water. Finally, a dark green precipitate of pure CuWO$_4$ NPs was produced by drying the washed CuWO$_4$ sample at 200 °C for two h before grinding it into powder.

2.2 Preparation of PVP/Cs/ CuWO$_4$ nanocomposite

Cs powder (˃ 70% deacetylated) of molecular weight (M$_W$) ~ 1.1 × 10^5 g/mol., PVP of k = 30, and M$_W$ = 4 × 10^4 g/mol., were used to prepare the PVP/Cs blend. 1.0 g of Cs was dissolved in 75 ml of 2 wt% acetic acid (CH$_3$COOH) using magnetic stirring for 2 h. 0.25 g of PVP in 20 ml distilled water solution was added to this solution, and the stirring continued for one hour at RT. The obtained homogeneous solution was cast into Petri dishes of diameters of ~ 10 cm. For CuWO$_4$/PVP/Cs PNC, the desired mass x (1.0, 3.0, and 5.0%) of CuWO$_4$ was calculated according to the following equation:

$$x(\%) = \frac{W_{filler}}{W_{filler} + 1.25},\qquad (1)$$

where W_{filler} is the mass of CuWO$_4$ and "1.25" in the denominator is the total mass of the polymers (PVP + Cs). The calculated W_{filler} was dissolved in distilled water using an ultrasonic bath and magnetic stirring and then added to the PVP solution. The films' composition is summarized in Table 1. The Petri dishes were put on leveled plates and left to dry at 45 °C for ~ 2 days. When removing the films, care was taken to

Table 1 The weight of PVP, Cs, and CuWO$_4$ in each film

Film	Composition (g)	
	PVP/Cs	CuWO$_4$
PVP/Cs	0.25/1.0	–
1.0 wt% CuWO$_4$	0.25/1.0	0.0126
3.0 wt% CuWO$_4$	0.25/1.0	0.0386
5.0 wt% CuWO$_4$	0.25/1.0	0.0657

obtain films with uniform thickness for optical and dielectric measurements.

2.3 Characterization

The surface morphology and elemental composition of CuWO$_4$ and CuWO$_4$/PVP/Cs PNC films, the cross-section, and film thickness were studied using field emission-scanning electron microscopy (FE-SEM; Carl ZEISS Sigma 500 VP, coupled with EDS). The X-ray diffraction patterns of CuWO$_4$ and CuWO$_4$/PVP/Cs were recorded using XRD Shimadzu 6000 diffractometer, in the 2θ range of 4°–90°, with a Cu K_α source of wavelength λ = 1.5406 Å. The vibrational modes of the samples were studied using Fourier transform infrared (FTIR) spectroscopy (JASCO, FT/IR-6200) in the wavenumber range 4000–400 cm^{-1}.

The water uptake (WA %), the porosity (P %), and the density (ϱ, g/cm^3) were investigated using a piece of dimensions (1 cm × 1 cm) from each sample. From the dry (W_d) and wet (Ww) weights of the sample, the ϱ (g/cm^3), WA (%), and P (%) were measured using the following relations [21–26]:

$$\rho = \frac{W_d}{(W_w - W_o)}\rho_{w'},\qquad (2)$$

$$WA\% = \frac{(W_w - W_d)}{W_d} x100,\qquad (3)$$

$$P\% = \frac{(W_w - W_d)}{(W_w - W_o)} x100,\qquad (4)$$

where ϱ_w = 1 g/cm^3 and W_o is the initial weight of the sample.

Optical measurements (absorbance, transmittance, and reflectance) were evaluated using a Shimadzu UV-3600 UV–VIS–NIR spectrophotometer at room temperature (RT) and in the wavelength range 200–1600 nm, with an accuracy of ± 0.2 nm.

The dielectric constant (ϵ'), loss tangent ($\tan\delta$), and ac conductivity (σ_{ac}) were measured in the frequency range 200 Hz–8 MHz and temperature range 293–393 K, using a Hioki model 3532 High Tester LCR (Ueda, Nagano, Japan), with a highly accurate and stable capacitance measurement of the order of 1.0×10^{-4} pF. The following equations were used:

$$\epsilon'(\omega) = C_p d / \pi r^2 \epsilon_o, \tag{5}$$

$$\tan\delta = \frac{\epsilon''}{\epsilon'}, \tag{6}$$

$$\sigma_{ac} = \epsilon_0 \omega \epsilon'', \tag{7}$$

where d denotes the thickness of $CuWO_4$/PVP/Cs film, r represents the radius of $CuWO_4$/PVP/Cs film contact area, $\epsilon_o = 8.854 \times 10^{-12}$ F/m is the dielectric permittivity of the air, C_p is the capacitance, and ϵ'' is the dielectric loss.

3 Results and discussion

3.1 Structural and morphological properties

The XRD pattern of the co-precipitated $CuWO_4$ is shown in Fig. 1a. In this pattern, the peaks at $2\theta = 15.06°$, $18.92°$, $22.88°$, $24.01°$, $25.82°$, $28.58°$, $29.32°$, $30.06°$, $32.04°$, $35.54°$, $36.73°$, $38.91°$, and $55.5°$ are indexed to the (010), (100), (110), (011), $(\bar{1}01)$, $(\bar{1}\bar{1}1)$, (111), (020), $(\bar{1}11)$, (002), (021), $(\bar{1}20)$, and $(\bar{1}\bar{1}1)$, respectively, of $CuWO_4$. Other peaks of fewer intensities and their corresponding to Miller indices are shown in Fig. 1a. This pattern corresponds to the triclinic (an orthic) phase of $CuWO_4$ (SG: $P1$) and is consistent with the data of JCPDS file 88–0269 [9, 13]. The high intensity and narrow width of the XRD peaks indicate the crystallization quality of the $CuWO_4$ [27]. Considering the three major peaks at $29.32°$ (111), $28.58°$ $(\bar{1}\bar{1}1)$, and $32.04°$ $(\bar{1}11)$ of relative intensities of 100, 28, and 27% and full-width at half maximum intensity (β) of 0.166, 0.233, and 0.174, respectively, the crystallite size D was evaluated using the well-known Scherrer equation: $D = \frac{0.9 \times 0.154(nm)}{\beta\cos(\theta)}$, where 0.154 nm is the wavelength (λ) of the used Cu K_α radiation. The calculated D values were in the range of 32.38–49.44 nm and $D_{av} = 43.1$ nm. Similarly,
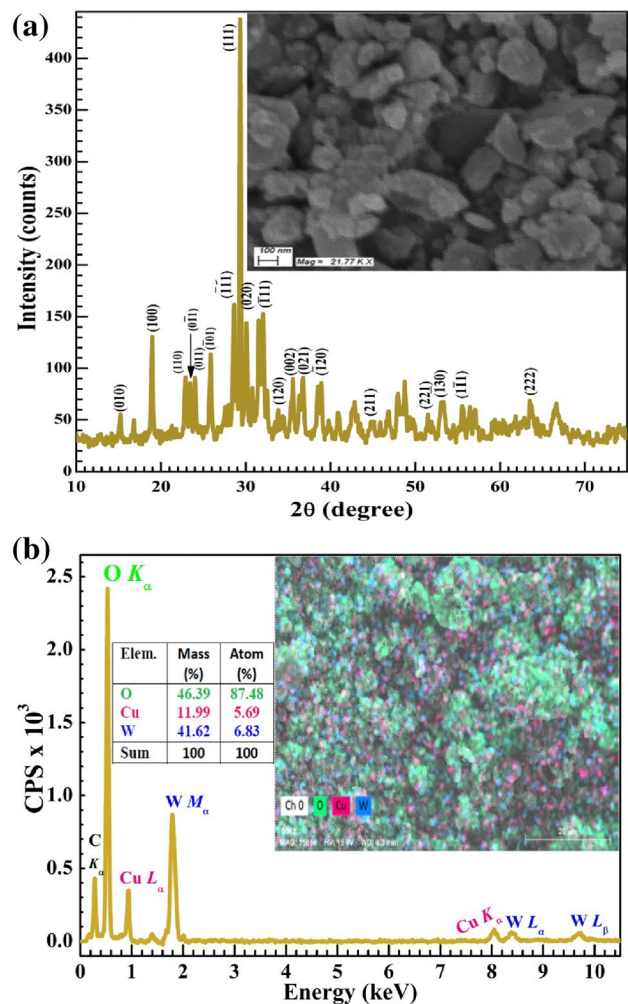

Fig. 1 **a** XRD of $CuWO_4$ NP and FE-SEM (the inset) and **b** EDX spectrum of $CuWO_4$ and elemental composition and mapping (the insets)

Thiruppathi et al. [6] prepared $CuWO_4$ with $D_{av} = 44$ nm, using 0.1-M $CuCl_2$ and $Na_2WO_4.2H_2O$ via a hydrothermal process.

The inset of Fig. 1a shows the FE-SEM image of $CuWO_4$ that seems as particles of various sizes in the range of 50–150 nm. This value is bigger than D_{av} given by XRD. This difference is because SEM gives the particle or grain size, while each grain may contain several crystallites. For the sol–gel prepared Y_2O_3 NPs the grain size was slightly smaller than 100 nm and D_{av} was in the range of 18.4–19.5 nm [28]. Figure 1b shows the EDX spectrum of $CuWO_4$ and the mass (%) and atom (%) ratios of O, W, and Cu are listed in the inserted table. The sample is composed of (i) 87.48% oxygen, where the O K_α line appears at
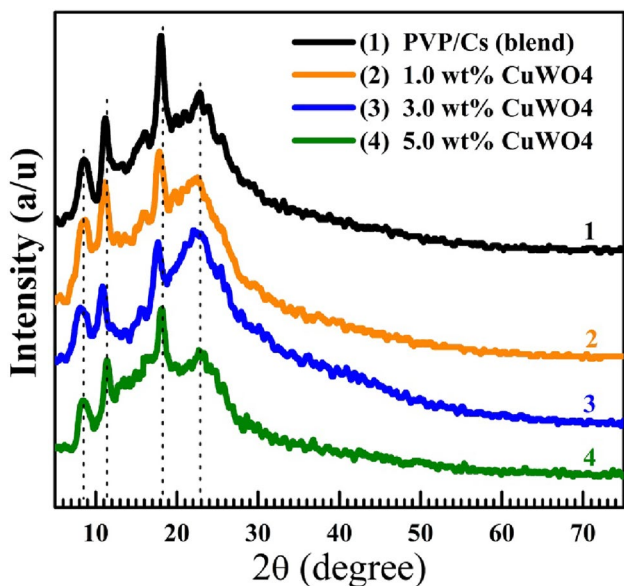
Fig. 2 XRD patterns of PVPCs and CuWO$_4$/PVP/Cs nanocomposites

Fig. 3 EDX spectra of PVPCs loaded with 1.0- and 3.0-wt% CuWO$_4$ nanoparticles

~ 0.5 keV, (ii) 6.83% tungsten, where W M_α, W L_α, and W L_β emission lines appear at ~ 1.78, 8.4, and 9.7 keV, respectively. (iii) The Cu represents 5.96% where its L_α and K_α lines are at 0.93 and 8.05 keV, respectively. The C K_α line appears at 0.27 keV arising from the carbon grid and the holder of the sample. The O, W, and Cu atoms are uniformly distributed through the whole sample, as indicated by the elemental mapping inserted in Fig. 1b and Fig. S1 (see the supplementary materials file).

Figure 2 shows the X-ray diffraction patterns of PVP/Cs and CuWO$_4$/PVP/Cs PNC. The pure blend exhibits characteristic peaks at $2\theta \approx 8.5°$, $11.2°$, $18.1°$, and $22.85°$. The first three peaks indicate the existence of crystalline or arranged regions in the blend, which could arise due to the intramolecular interaction between the OH and NH$_2$ groups in the blend [29]. However, the wide peak at $2\theta = 22.85°$ belongs to the amorphous phase [30, 31]. Three main notes here: (i) the blend has a semi-crystalline nature. (ii) CuWO$_4$ has been distributed effectively in the amorphous regions of the blend and the XRD instrument is not able to detect this nanofiller. (iii) The intensity of the crystalline peaks decreased, and the wide of the amorphous peak increased with increasing CuWO$_4$ loading. The crystallinity degree $X_C\% = \frac{A_c \times 100}{A_c + A_a}$, where A_c and A_a are the areas under the crystalline and amorphous peaks, respectively. X_c of the pure blend is 18.5% decreased
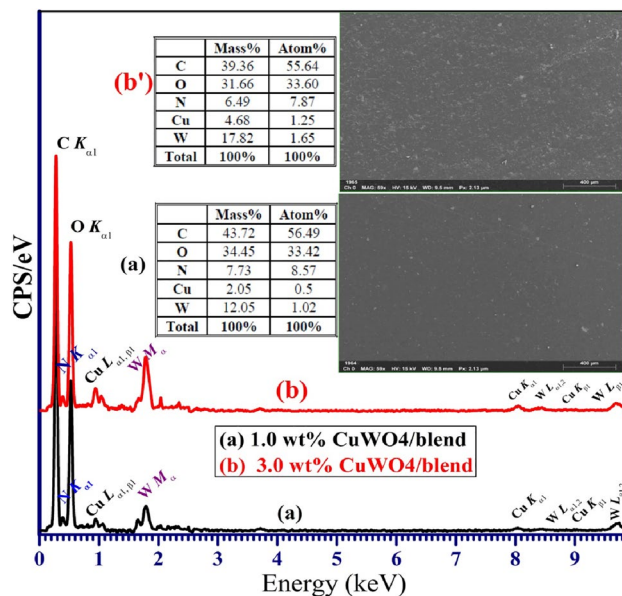
to 12.6% at 1.0-wt% CuWO$_4$ loading and marginally decreased till 10.4% with the further increase in CuWO$_4$ ratio 5.0 wt%. This decrease in X_C indicates increasing the biodegradability of the blend loaded with CuWO$_4$ [32], and the blend flexibility and chain motion which in turn will improve the conductivity of the material.

Figure 3 shows the EDS spectra, chemical (elemental) composition, and the inset tables of PVP/Cs loaded with 1.0- and 3.0-wt% CuWO$_4$. In the two samples, the main components are C (55.64–56.49 at%), O (33.42–33.60 at%), and N (7.87–8.57%). These ratios are consistent with the chemical structure of both Cs (C$_{56}$H$_{103}$N$_9$O$_{39}$)$_n$ and PVP (C$_6$H$_{10}$NO)$_n$. Although XRD did not detect any peaks for CuWO$_4$, EDX confirmed the existence of Cu (0.5–1.25 at%) and W (1.02–1.65 at%). The Cu appears at 0.93 keV ($L_{\alpha1}$), 0.95 keV ($L_{\beta1}$), 8.05 keV ($K_{\alpha1}$), and 8.9 keV ($K_{\alpha1}$). The W emissions appear at 1.85 KeV (M_α), 8.4 keV ($L_{\alpha1}$), and 9.7 keV ($L_{\beta1}$). This result confirms the successful incorporation of CuWO$_4$ inside PVP/Cs chains. Moreover, the inserted tables and SEM images confirm the homogeneous distribution and increase of [Cu] and [W] with increasing CuWO$_4$ doping ratio. To shed more light on the surface morphology of pure and CuWO$_4$/PVP/Cs films, FE-SEM images were captured and presented as shown in Fig. 4a–c. PVP/Cs have a smooth, homogeneous, and crack-free surface, Fig. 4a. This means the
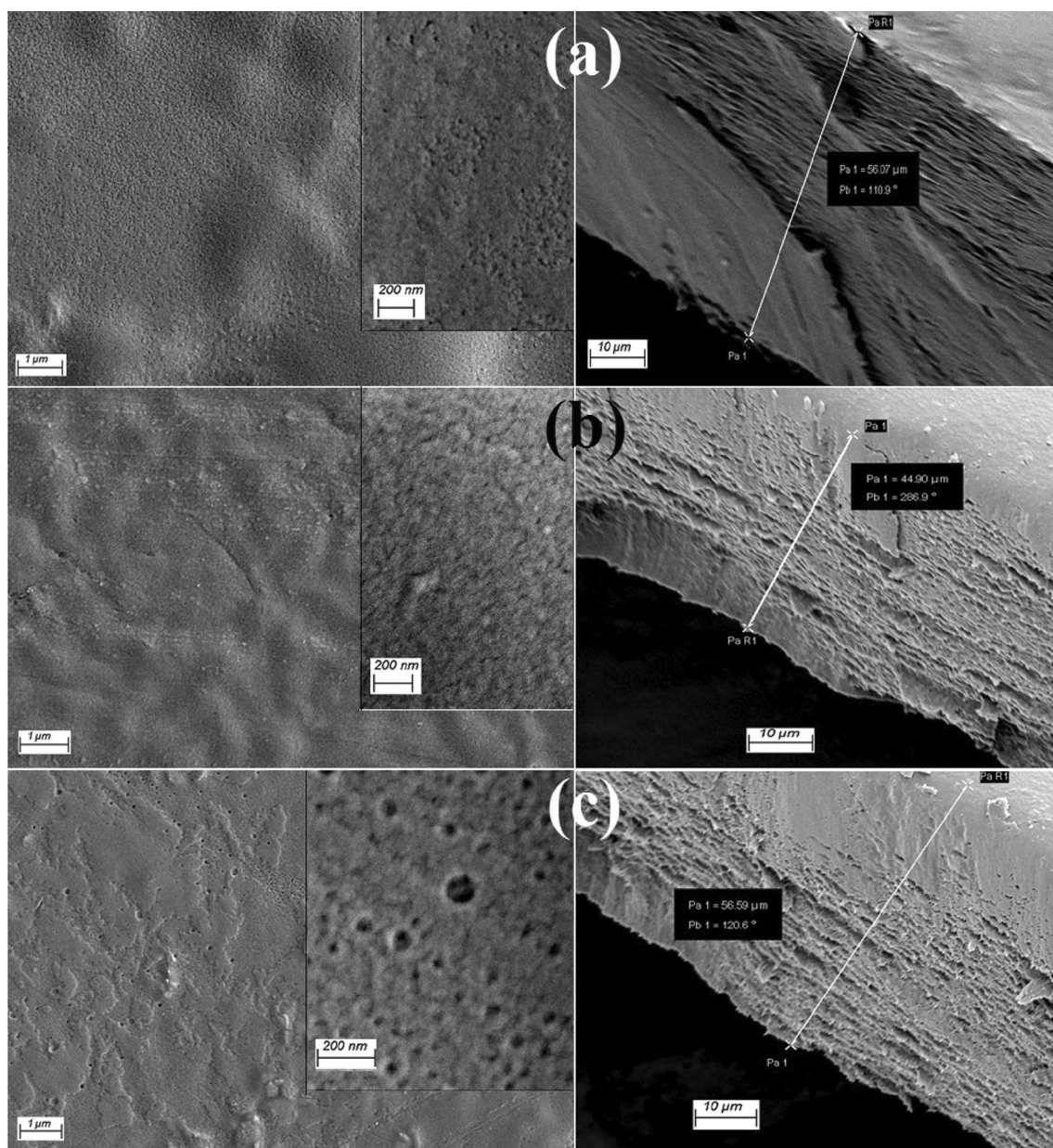
Fig. 4 FE-SEM images for pure and PVP/Cs loaded with 3.0- and 5.0-wt% $CuWO_4$.

homogeneity and complete miscibility of PVP and Cs polymers. At higher magnification, a very large number of nanopores exist on the film's surface. In addition, the cross-sectional investigation emphasizes that these pores do not exist inside the blend. Loading of 3.0- and 5.0-wt% $CuWO_4$ was uniformly distributed into the blend matrix but induced some heterogeneity and the surface became rougher. These fillers encourage the pores to form on the surface and inside the matrix, with uniform distribution, as seen in the insets of Fig. 4b and c. Moreover, the films have a thickness

range of 45–57 μm. The induced structural changes could influence other physical properties such as the values of ρ, P %, and WA% of the PNC.

The influences of $CuWO_4$ content on WA %, P %, and ϱ are shown in Fig. 5. The WA % of $CuWO_4$/PVP/Cs decreases from 216.9 to 80.66% with increasing $CuWO_4$ nanofillers loading from 0.0 to 5.0 wt%. This reduction in WA% may be due to the hydrophobic characteristics of the added metal oxide ($CuWO_4$) [21, 22]. The strong adhesion of $CuWO_4$ nanofiller at the PVP/Cs interfaces leads to increasing the
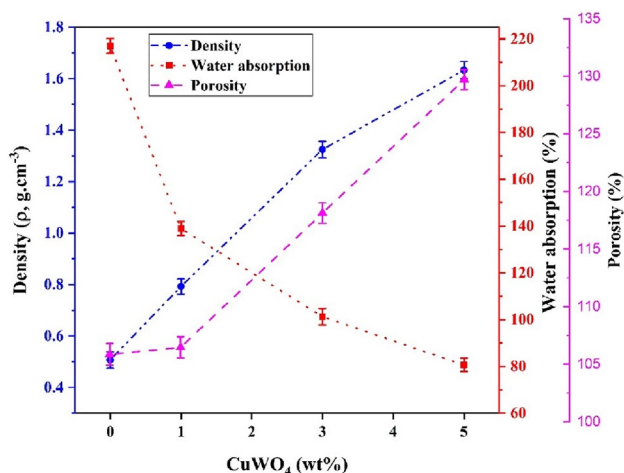
Fig. 5 The water absorption, porosity, and density of CuWO$_4$/PVP/Cs.

porosity from 105.86, for the pure blend, to 129.71% for the blend loaded with 5.0-wt% CuWO$_4$ [23]. This is consistent with the observation of FE-SEM, Fig. 4. Additionally, incorporation of this dense metal oxide (ρ_{CuWO4} = 7.48 g/cm^3) result in increasing the ρ of CuWO$_4$/PVP/Cs PNC from 0.507 to 1.633 g/cm^3. Similar results were reported in [24–26].

3.2 FTIR spectra of CuWO$_4$ and PVP/Cs PNC

FTIR is a powerful and interesting tool to clarify the vibration modes of the material functional groups and the interaction/complexation of the blend chains with the added nanofiller. FTIR spectra were recorded at RT and are shown in Fig. 6. The spectrum of CuWO$_4$ displays several absorption peaks. This material can adsorb the water vapor from the surrounding [27], where the bands at ~ 3430 and 1640 cm^{-1} are ascribed to the –OH stretching and H–O–H bending vibrations. The band at 610 cm^{-1} could be assigned to the Cu–O stretching in the triclinic CuWO$_4$. The bands at 729 and 812 are assigned to the stretching modes of O–W–O/ W–O–W groups. In addition, the bands at 472 and 903 cm^{-1} are assigned to the stretching vibration of WO$_4$ tetrahedra [6, 10, 33]. This result indicates the high purity of our co-precipitated CuWO$_4$.

The spectra of CuWO4/PVP/Cs PNC contain a wide and broadband in the range of 3000–3600 cm^{-1}, which can be divided into two bands, as shown in Fig. 6; the first centered at 3360 cm^{-1} can be assigned

to the asymmetrical stretching of N–H group in the PVP/Cs blend [34], and the second is centered at 3265 cm^{-1} arising from the OH stretching vibration overlapping with the symmetric stretching o N–H through the carbohydrate ring in the C$_S$ [1, 4]. Similarly, the two bands at 2935 and 2875 cm^{-1} arise from the C–H symmetric and asymmetric stretching vibrations in the CH$_2$ groups [35]. The absorption band at 1650 cm^{-1} is attributed to the –C=O stretching of amide I in Cs. The relatively broad and strong band at 1547 cm^{-1} can be assigned to the symmetric deformation of $-NH_3^+$ (resulting from the ionization of NH$_2$ groups by adding acetic acid during the dissolving Cs) [36]. In addition, the stretching vibration of –C=N of amide-III in Cs appears at 1397 cm^{-1} [35]. The small absorption band at 1290 cm^{-1} is owing to the frequencies of (CH + OH) combination [37]. The three absorption bands at 1150 cm^{-1}, 1068 cm^{-1}, and 1025 cm^{-1} can be ascribed to the asymmetric stretching vibration of C–O–C and the stretching of C–O in the C–OH groups [18]. The small band at 647 cm^{-1} may be owing to twisting vibrations in the blend [38]. All films have similar spectra and no obvious shift in the peak position due to CuWO$_4$ incorporation. However, it is seen that the width and intensity of the peaks decreased after loading 1.0-wt% CuWO$_4$ but increased with increasing the ratio of the filler to 3.0 and 5.0 wt%. This result indicates
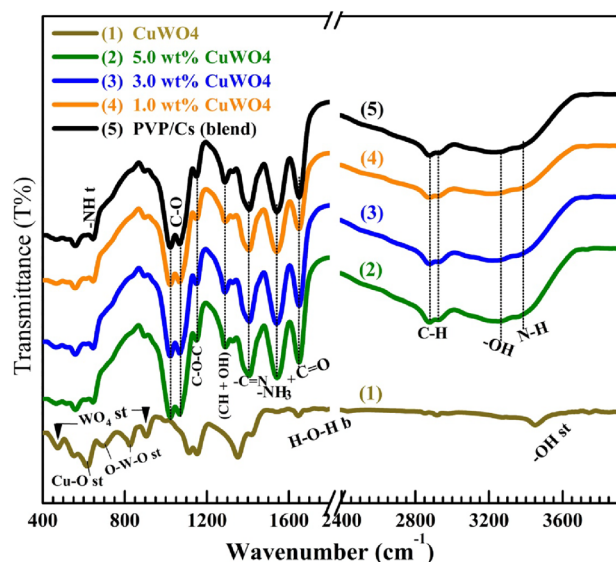

Fig. 6 FTIR transmittance spectra of CuWO$_4$, PVPCs, and CuWO$_4$/PVP/Cs PNC.

that 1.0 wt% is the more effective ratio in restricting the vibrations of PVP/Cs blend functional groups.

3.3 UV–vis study and optical constants

Investigating the optical properties of semi-crystalline materials and determining their optical constants are important for elucidating the electronic and band structures for optical communication and device fabrications. Figure 7a and b shows the absorption index ($k = \frac{\alpha\lambda}{4\pi}$) and transmittance spectra (T%) of the CuWO$_4$/PVP/Cs PNT, where $\alpha = \frac{2.303 Abs.}{d}$ and d is the film thickness. The films show low k values ($k \leq 2.0 \times 10^{-3}$), Fig. 7a. The PVP/Cs show two weak absorption peaks at 278 and 310 nm, assigned to $\pi \rightarrow \pi^*$ and $n \rightarrow \pi^*$ transitions, respectively, that are arising due to the existence of unsaturated bonds [39]. The intensity of these two peaks is significantly improved after doping with 1.0-wt% CuWO$_4$ and then decreased and left-shifted with increasing loading ratio of CuWO$_4$ to 3.0 and 5.0 wt%. This results from the induced changes in X$_C$% of the PVP/Cs after mixing with CuWO$_4$ [40], as shown in XRD results. For comparison purposes, the value of T% at 600 nm of all samples is listed in Table 2. At $\lambda \geq 600$ nm, the PVP/Cs show a motivating T% in the range of 85–90%, Fig. 7b. The PNC films have $T = 57\%$ at $\lambda = 600$ nm. In the studied λ range, 1.0-wt% CuWO$_4$/

PVP/Cs film exhibits a maximum T of 78% decreases to 68% with increasing the ratio of the filler to 5.0 wt%. With decreasing the λ toward the UV region, the T% of the films decreases sharply, and the absorption edge shifts to higher λ especially at 1.0-wt% doping, indicating a narrowing of the optical band gap of the blend. The T% values of the films emphasize the homogeneity and CuWO$_4$/PVP/Cs composites and their convenience for optical devices.

Using Tauc's relations: $(\alpha h\upsilon)^{1/m} = A(h\upsilon - E_g)$ [4], where $h\upsilon$ is the incident photon energy ($\sim \frac{1242(eV)}{\lambda(nm)}$), C is a constant, $m = \frac{1}{2}$ or 2 for allowed direct and indirect transitions, respectively, and the direct (E_g^{dir}) and indirect (E_g^{ind}) optical band gap can be determined. Figure 8a and b shows the $(\alpha h\upsilon)^2$ vs. $h\upsilon$ and $(\alpha h\upsilon)^{1/2}$ vs. $h\upsilon$. Extrapolating the linear parts of these plots to $\alpha = 0$, gives the E_g^{dir} and E_g^{ind} values which are listed in Table 2. PVP/Cs blend has E_g^{dir} and E_g^{ind} of 5.0 and 4.2 eV, respectively, significantly reduced to 4.4 and 3.1 eV after loading 1.0-wt% CuWO$_4$. However, increasing the content of the filler to 5.0 wt% widens the E_g^{dir} and E_g^{ind} of PNC films to 4.8 and 3.8 eV, respectively, but still lower than the values of the pure blend. In the previous work, the incorporation of 2.0-wt% hematite nanorods narrowed the E_g^{dir} of PVP/Cs from
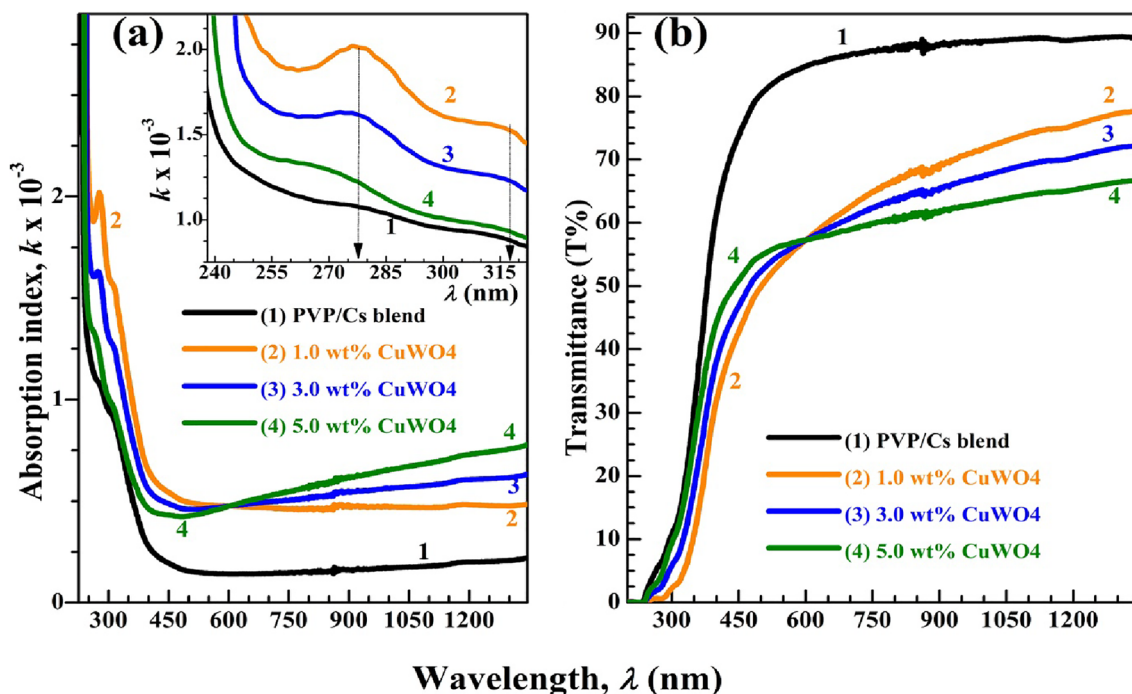

Fig. 7 UV–vis–NIR spectra of CuWO$_4$/PVP/Cs: **a** absorption index (k) and **b** transmittance (T%)
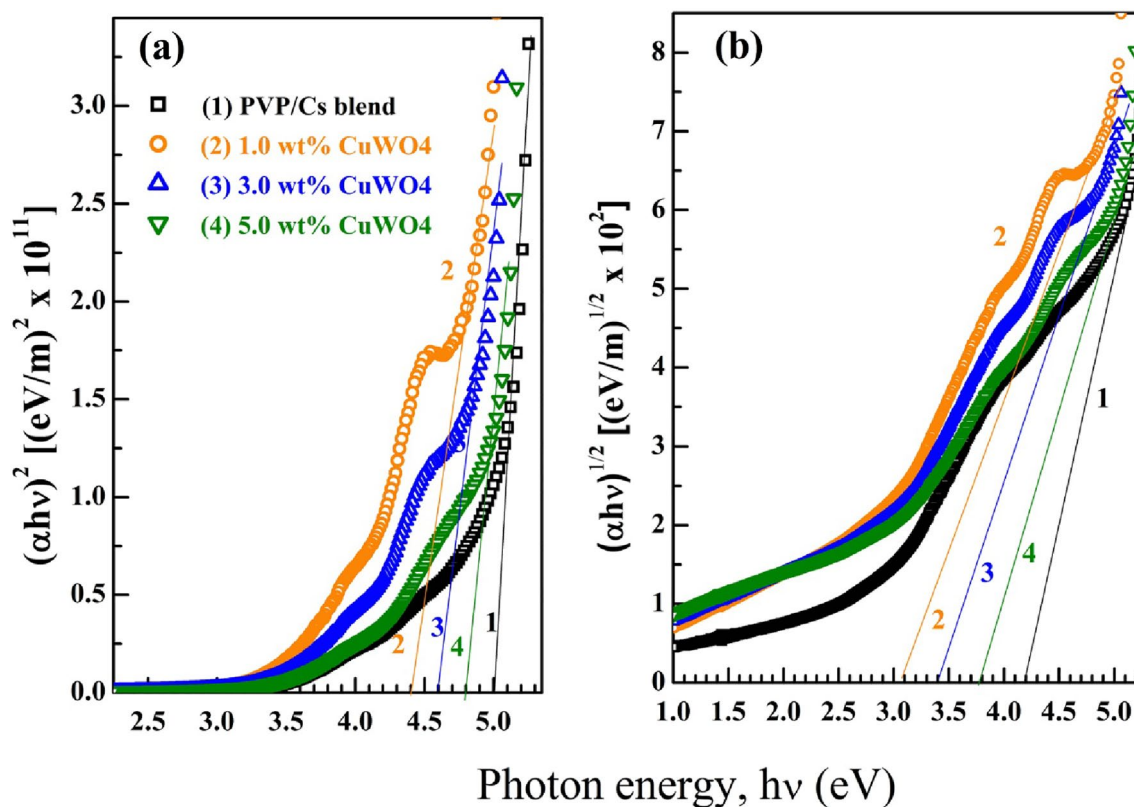
Fig. 8 Applying Tauc's relation to determine **a** direct and **b** indirect E_g of CuWO$_4$/PVP/Cs.

Table 2 Optical properties of CuWO$_4$/PVP/Cs: band gap (E_g), reflectance (R%), refractive index (n), and the ratio of carriers concentration to the electron effective mass (N/m^*)

Film	E_g^{dir} (eV)	E_g^{ind} (eV)	R% (600 nm)	n (600 nm)	$\frac{N}{m^*}\left(\frac{e^2}{\pi c^2}\right)$ (nm^{-2})
PVP/Cs	5.0	4.2	8.08	1.79	1.96×10^{-7}
1.0-wt% CuWO4	4.4	3.1	15.36	2.29	1.37×10^{-6}
3.0-wt% CuWO4	4.6	3.4	23.23	2.86	1.06×10^{-6}
5.0-wt% CuWO$_4$	4.8	3.8	15.96	2.33	6.52×10^{-7}

5.4 eV to 4.05 eV [1]. Abdelghany et al. [20] reported E_g^{dir} and E_g^{ind} of about 4.77 and 4.14 eV for a blend composed of PVP (80%)/Cs (20%) which widened to 4.9 and 4.47 eV, respectively, after doping with 0.002 g of ZnS NP. CuWO$_4$ filler (E_g = 2.2–2.4 eV) forms a semiconducting network inside the blend and create defects, charge transfer complexes, as well as create localized states in the forbidden region between the conduction and valence bands of the blend. This results in the observed shrinkage in E_g. However, increasing the filler content beyond 1.0 wt% may reduce the efficiency of this network due to the agglomeration of the nano-sized filler owing to its huge surface energy.

Evaluating the index of refraction (n) of the materials is essential for optical device applications. The recorded reflectance (R%) and ($n = \frac{1+\sqrt{R}}{1-\sqrt{R}}$ [41]) of the films are shown in Fig. 9a and b. Both R% and n decrease with λ in the UV region. In the visible region, the added CuWO$_4$ filler made the R% and n behavior take a bell shaped. Insertion of CuWO$_4$ inside PVP/Cs improves its reflectivity due to the scattering effect of the dispersed particles. CuWO$_4$/PVP/Cs PNC has a high n and may be utilized in some top-end advanced optoelectronic equipment, such as light-emitting diodes, waveguides, and anti-reflective coatings. Considering the dispersion relation: $n^2 = \epsilon_l - \left(\frac{e^2}{\pi c^2}\right)\left(\frac{N}{m^*}\right)\lambda^2$ [1], where ϵ_l, e, c, and $\frac{N}{m^*}$ are the dielectric constant of lattice, electron charge, speed of light, and the ratio of carrier concentration
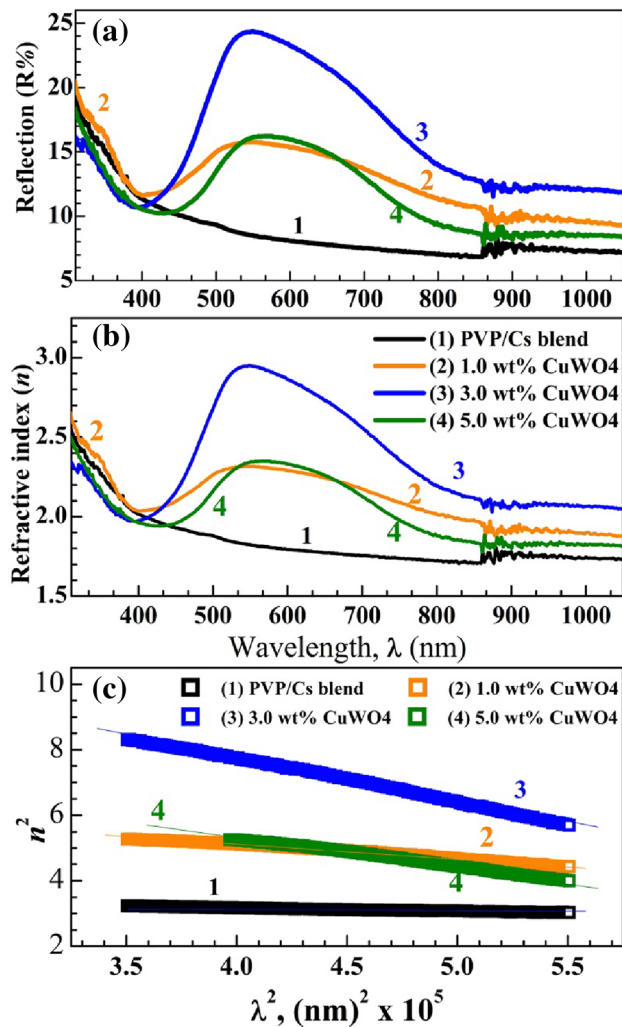
Fig. 9 **a** Reflection (R%), **b** refractive index (n), and **c** n^2 and λ^2 to determine (N/m^*)

to the effective mass of the electron, respectively. The $\frac{N}{m^*}$ value can be easily from the plot of n^2 vs. λ^2 as shown in Fig. 9c. The slope of straight lines gives the values of $\frac{N}{m^*}\left(\frac{e^2}{\pi c^2}\right)$ as listed in Table 2. The value of $\frac{N}{m^*}\left(\frac{e^2}{\pi c^2}\right)$ increased from 1.96×10^{-7} to 1.37×10^{-6} nm^{-2} after loading 1.0-wt% CuWO$_4$ into the blend but slightly reduced to 1.06×10^{-6} and 6.52×10^{-7} nm^{-2} with increasing the content of the filler to 3.0 and 5.0 wt%, respectively. The observed change in $\frac{N}{m^*}\left(\frac{e^2}{\pi c^2}\right)$ is consistent with the variation in E_g^{dir} and E_g^{ind} of PNC films, where increasing/decreasing carrier concentration results in decreasing/increasing the E_g values. Moreover, these results indicate that the optical properties of the PVP/Cs blend can be tuned by the ratio of CuWO$_4$ nanofiller. These enhancements in

the optical properties make these compositions suitable for optoelectronic devices, such as organic light-emitting diodes and photovoltaic cells [42].

3.4 Dielectric constant and loss of CuWO$_4$/PVP/Cs

Improving the dielectric property of a material by increasing the number of charges it can store is essential for device applications, such as supercapacitors and batteries. Figure 10a–d and Fig. S2 exhibit the variation of PVP/Cs dielectric constant (ε'), before and after loading of 1.0–5.0-wt% CuWO$_4$, at temperatures (293–393 K) and frequencies ($f = 2.0$ kHz–4.0 MHz). Increasing the applied f results in a continuous decrease in the ε' values, Fig. S2. At low f, the accumulated charge carriers yield a high ε' and tend to build up a space-charge layer at the interface between the PVP/Cs film and the electrode, and any charge has the time required to change the direction according to the change in f-direction. However, increasing f is combined with a short periodic time in which the dipoles fail to reorient fast enough. Therefore, the dipolar polarization diminishes and may disappear and hence ε' values decrease [43, 44]. The temperature dependence is somewhat different. The curves (ε' vs. T) can be divided into two regions, in the first one, the ε' increases with increasing the temperature that supplies thermal energy enough to free localized dipoles which in turn align themselves in the f-direction. In the second region, the high temperatures increase the specific volume of the blend, hence the dipole concentration (dipole number/unit volume) decreases resulting in the observed decrease in ε'. The separation between the two regions is called the relaxation peak or the α-process, which shifts to the right with increasing the applied f. This α-process is assigned to the micro-Brownian motion along the PVP/Cs main chains found in its amorphous regions.

Two additional notes on the behavior of ε': (i) the dispersion of the curves at a lower temperature is higher than that at higher temperatures. This means f has the decisive effect at low temperatures, and this effect reduces at a higher temperature, after the α-process. (ii) At low temperatures, the PVP/Cs blend has ε' in the range of 8.3–17.8 that significantly increased to 9.8–24.5 after loading 1.0-wt% CuWO$_4$, where the heterogeneity created inside the blend and the contribution of the interfacial polarization
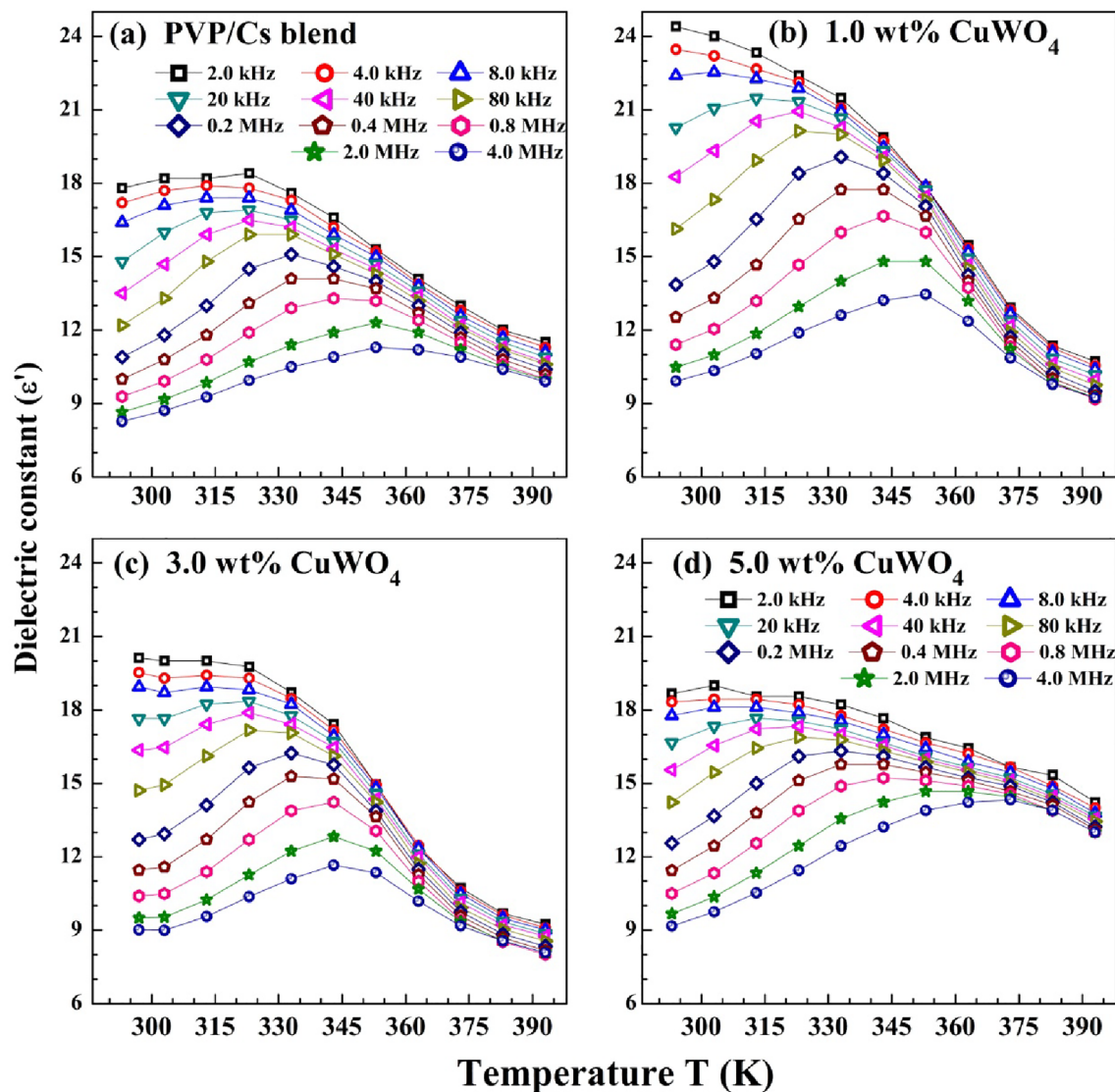
Fig. 10 Dependence of dielectric constant of PVP/Cs on the temperature at different f and $CuWO_4$ (0–5.0 wt%)

increase ε'. However, a further increase in the added $CuWO_4$ ratio decreases the ε' range to 9.0–19, but still higher than that of the pure blend. The higher filler content may not be distributed uniformly and induce structural changes that act as trapping centers for the charges.

The dependence of the dielectric loss (ε'') with f at different temperatures is given in Fig. 11a–d and Fig. S3. At the low f (≤ 40 kHz), the ε'' is small and decreases with increasing temperatures up to a certain limit (the gained thermal energy is small and cannot affect the motion of the PVP/Cs chains) then increases with temperature (the temperature above a certain limit improves the motion of the chains and rise ε'').

At higher f (≥ 0.2 MHz), ε'' increases with increasing temperature till a certain limit then decreases with further increase in the temperature, where the free charge carriers, the polar groups in the blend, and the motion of the chain become fail to in phase with the oscillating f. Moreover, the observed relaxation peaks in the PVP/Cs and $CuWO_4$/PVP/Cs spectra shifted to higher f with increasing temperature, Fig. 11, or shifted to higher temperatures with increasing f, Fig. S3. The higher values of ε'' at $f > 1.0$ MHz is a result of increasing the molecular vibrations in the crystalline regions in the PVP/Cs blend [45]. In the middle region of the studied frequencies (3.0 kHz $\leq f \leq 1.0$ MHz), the maximum values of ε'' for PVP/Cs and 5.0-wt%
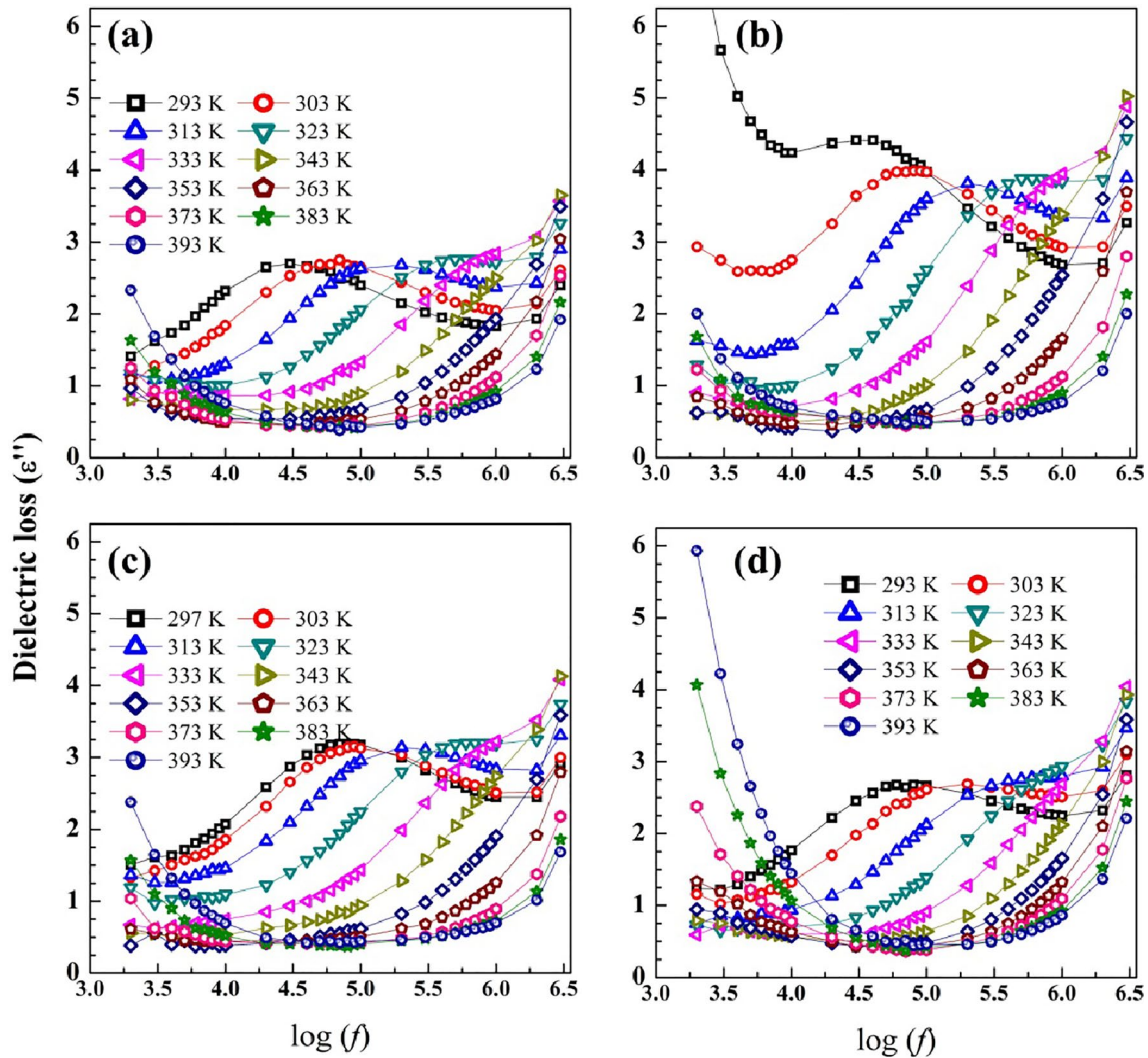
Fig. 11 Variation of dielectric loss of PVP/Cs on f at different temperatures and CuWO$_4$ (0–5.0 wt%)

CuWO$_4$/PVP/Cs the blend is around 2.75 regardless of the temperature. Increases slightly to 3.0 and ~ 4 for 3.0- and 1.0-wt% CuWO$_4$/PVP/Cs, respectively. This may indicate the fact that the crystalline regions in this semi-crystalline blend dissolve effectively in their amorphous regions with increasing temperature [46]. Incorporation of CuWO$_4$ into PVP/Cs blend improved ε' significantly maintaining similar ε'' values. These composites, therefore, can be further improved to be suitable for batteries and supercapacitors (energy storage devices), and the electrostriction systems utilized in the artificial muscles [47]. Moreover, 1.0-wt% CuWO$_4$/PVP/Cs has the higher ε' and therefore the higher dielectric displacement ($D = \epsilon_o \epsilon' E$) and high energy density ($U_e = \int E dD$), in the presence of the applied electric field E [48].

The conductivity (σ_{ac}) of the dielectric materials (, $\omega = 2\pi f$ is the angular frequency) is related to the temperature by the Arrhenius equation: , where k_B is the Boltzmann constant, σ_o is a pre-exponential factor, E_a is the activation energy, and T is the temperature (K). The conductivity of pure and 1.0-wt% CuWO$_4$-doped PVP/Cs and the log (σ_{ac}) vs. 1000/T are shown in Fig. 12. The σ_{ac} of PVP/Cs is in the order of 1.2×10^{-6}–7.3×10^{-4} S/m and this high σ_{ac} may be due to the polycationic characteristic of the blend. The NPs of CuWO$_4$ semiconductor may form 3D connected networks inside the blend where the σ_{ac} range of 1.0-wt% CuWO$_4$/PVP/Cs increased to 4.95×10^{-6}–9.16×10^{-4} S/m. The σ_{ac} curves could be divided into two regions showing an Arrhenius behavior; in the region I, the conductivity improvement is due to the available thermal activation
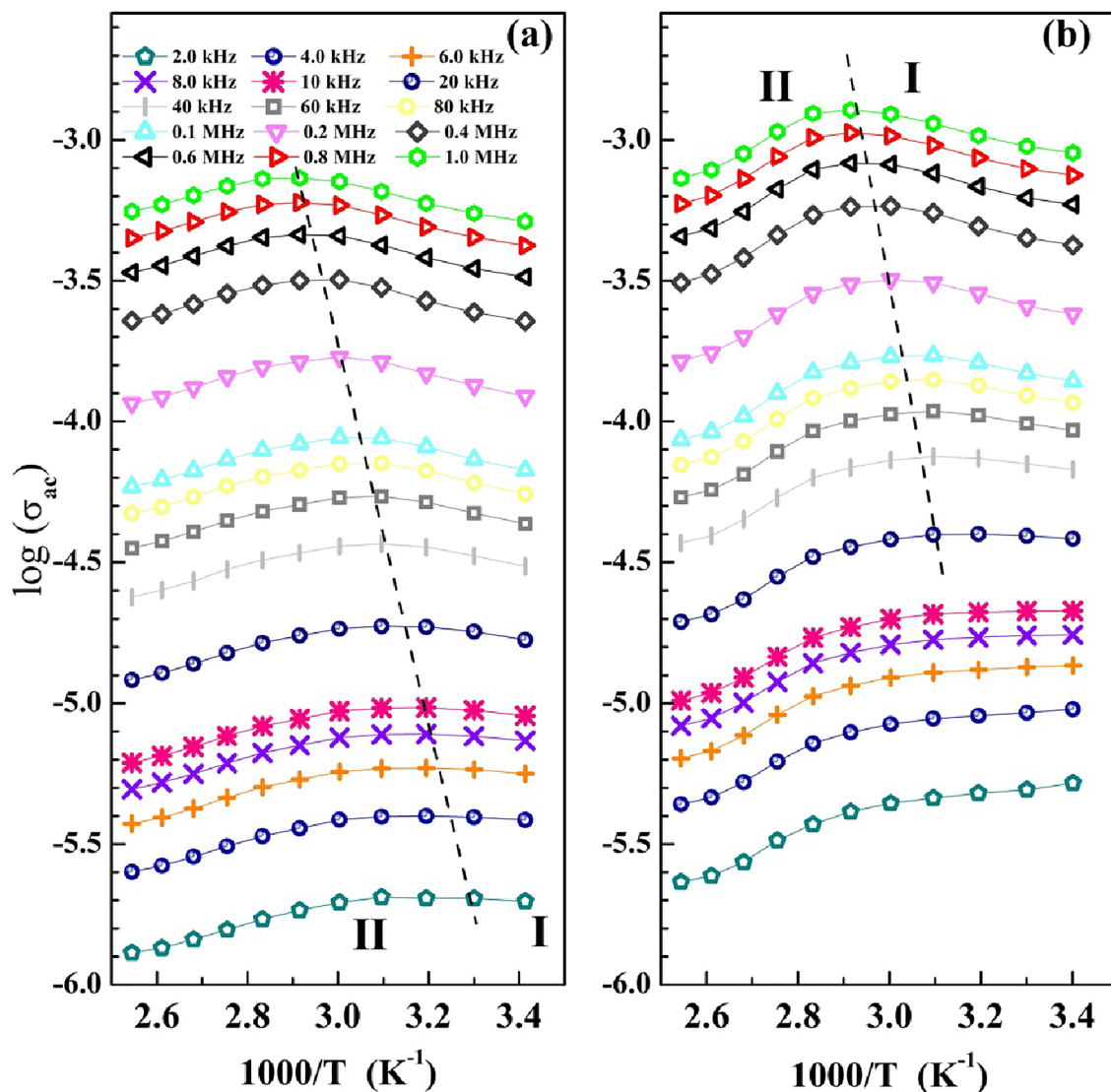
Fig. 12 Log (σ_{ac}) vs. 1000/T for pure and 1.0-wt% CuWO$_4$-doped blend

of the PVP/Cs polymeric chains. The decreasing trend with increasing T, in Region II, is related to the decrease in the carrier concentration and the structural changes in the blend with heating.

4 Conclusion

CuWO$_4$ NP and CuWO$_4$/PVP/Cs PNC were successfully prepared with co-precipitation and solution casting techniques. XRD and EDX showed the formation of CuWO$_4$ in the triclinic crystal structure with D_{av} = 43.1 nm, where the sample was found to composed of 87.48 at.% O, 6.83 at.% W, and 5.96 at.% Cu

with a uniform distribution. PVP/Cs is a semi-crystalline blend and X_C of the blend decreased from 18.5 to 10.4% after doping, where the EDX analysis confirmed the presence of both Cu and W in the blend. FE-SEM showed that the grain size of CuWO$_4$ is in the range of 50–150 nm. PVP/Cs has a crack-free surface and the incorporation of CuWO$_4$ NP induced some heterogeneity, roughness, and pores formation and increased both the density and porosity of the PVP/Cs. FTIR confirmed the high purity of CuWO$_4$ and the existence of all the reactive functional groups of the polymers, which were more restricted at 1.0-wt% CuWO$_4$ loading. The films exhibited small k values ($\leq 2.0 \times 10^{-3}$) and the transmittance of the

blend, which decreased from 85–90–68% at 5.0-wt% $CuWO_4$ doping ratio. Direct and indirect band gaps were decreased from E_g^{dir} and E_g^{ind} from 5.0 and 4.2 eV to 4.4 and 3.1 eV at 1.0 wt%, but then increased to 4.8 and 3.8 eV, respectively. Both the index of refraction and $\frac{N}{m^*}$ increased from 1.79 and 1.96×10^{-7} nm^{-2} to 2.29 and 1.37×10^{-6} nm^{-2} after doping with 1.0-wt% $CuWO_4$ and then decreased with increasing filler content. The ε' of PVP/Cs is in the range of 8.3–17.8, increased to 9.8–24.5 at 1.0-wt% filler content. The maximum values of ε'' for PVP/Cs and $CuWO_4$/PVP/Cs is small (2.75–4.0). The σ_{ac} increased from 1.2×10^{-6}–7.3×10^{-4} S/m to 4.95×10^{-6}– 9.16×10^{-4} S/m at 1.0-wt% filler content. In summary, the structural, optical, and dielectric properties can be controlled by $CuWO_4$ NP content. Therefore, these composites can be improved to be suitable for some energy storage devices such as supercapacitors as well as some optoelectronic applications, such as light-emitting diodes and photovoltaic solar cells.

Supplementary Information The online version contains supplementary material available at https://doi.org/10.1007/s10854-023-11118-x.

Author contributions

AMElS contributed to conceptualization; methodology; data curation; writing of the original draft; and editing of the manuscript. MIAAM contributed to conceptualization; methodology; data curation; investigation; writing of the original draft; and writing, reviewing, & editing of the manuscript. SMK contributed to data curation and writing of the original draft. ASA contributed to data curation; writing of the original draft; and writing, reviewing, & editing of the manuscript.

Funding

Data availability

Data will be made available on reasonable request.

Declarations

Conflict of interest The authors declare that they have no conflicts of interest.

Ethical approval Not required.

Consent to participate Not applicable.

Consent to publish Not applicable.

References

1. A.M. El Sayed, A.D.M. Mohamad, Synthesis, structural, thermal, optical and dielectric properties of chitosan biopolymer; influence of PVP and α-Fe_2O_3 nanorods. J. Polym. Res. **25**, 175 (2018). https://doi.org/10.1007/s10965-018-1571-x

2. P.H. Dinh, T.-D. Pham, D.Q. Trung, D.V. Thuan, N.T.D. Cam, N.T. Hanh, H.V. Ha, N.H.A. Thu, H.T. Trang, N.L.M. Tri, CuWO4 decorated by polypyrrole (PPy) protector/sensitizer for novel photocatalytic and stable water splitting for hydrogen generation. Int. J. Hydrogen Energy. **45**(41), 21442–21449 (2020). https://doi.org/10.1016/j.ijhydene.2020.05.229

3. J. Yesuraj, O. Padmaraj, S.A. Suthanthiraraj, Synthesis, characterization, and improvement of Supercapacitor Properties of $NiMoO_4$ nanocrystals with polyaniline. J. Inorg. Organ. Polym. Mater. **30**, 310–321 (2020). https://doi.org/10.1007/s10904-019-01189-x

4. A.M. El Sayed, S. El-Gamal, Synthesis, optical, and electrical properties of starch/chitosan/$NaTiO_3$ bio-nanocomposites modified with $ErCl_3$. Phys. Scr. **97**, 015805 (2022). https://doi.org/10.1088/1402-4896/ac40da

5. C. Nong, B. Yang, X. Li, S. Feng, H. Cui, An ultrasensitive electrochemical immunosensor based on in-situ growth of $CuWO_4$ nanoparticles on MoS_2 and chitosan-gold nanoparticles for cortisol detection. Microchem J. **179**, 107434 (2022). https://doi.org/10.1016/j.microc.2022.107434

6. M. Thiruppathi, K. Saravanakumar, M. Arunpandian, C. Ramalingan, E.R. Nagarajan, A novel $CuWO_4$-PMMA nanocomposite thin film as trouble-free and handpicking recoverable photocatalyst. https://doi.org/10.1080/03067319.2021.1951259

7. J.U. Lee, J.H. Kim, K. Kang, Y.S. Shin, J.Y. Kim, J.H. Kim, J.S. Lee, Bulk and surface modified polycrystalline $CuWO_4$ films for photoelectrochemical water oxidation. Renew. Energy. **203**, 779–787 (2023). https://doi.org/10.1016/j.renene.2022.12.129

8. L. Chen, S. Shet, H. Tang, K.-S. Ahn, H. Wang, Y. Yan, J. Turner, M. Al-Jassim, Amorphous copper tungsten oxide with tunable band gaps. J. Appl. Phys. **108**, 043502 (2010). https://doi.org/10.1063/1.3475714

9. A. Sarwar, A. Razzaq, M. Zafar, I. Idrees, F. Rehman, W.Y. Kim, Copper tungstate ($CuWO_4$)/graphene quantum dots (GQDs) composite photocatalyst for enhanced degradation of phenol under visible light irradiation. Res. Phys. **45**, 106253 (2023). https://doi.org/10.1016/j.rinp.2023.106253

10. G. Sun, Q. Gao, S. Tang, X. Chen, H. Liu, H. Gao, X. Zhao, A. Wang, X. Yu, S. Wang, Facile synthesis, Optical and Photoluminescence Properties of Copper Tungstate Phosphors with strong Near-Infrared Photoabsorption. Russ J. Phys. Chem. A **96**(6), 1348–1355 (2022). https://doi.org/10.1134/S0036024422060097

11. A. Hrubantova, R. Hippler, H. Wulff, M. Cada, O. Gedeon, P. Jiricek, J. Houdkova, J. Olejnicek, N. Nepomniashchaia, C.A. Helm, Z. Hubicka, Copper tungsten oxide (Cu_xWO_y) thin films for optical and photoelectrochemical applications deposited by reactive high power impulse magnetron co-sputtering. J. Appl. Phys. **132**, 215301 (2022). https://doi.org/10.1063/5.0123075

12. X. Du, Z. Dai, Y. Wang, X. Han, X. Zhang, Facile synthesis of MWO_4 (M = co, Ni, Zn and Cu) nanoarrays for efficient urea oxidation. Int. J. Hydrogen Energy. **47**, 8875–8882 (2022). https://doi.org/10.1016/j.ijhydene.2021.12.244

13. N. Jatav, J. Kuntail, D. Khan, A.K. De, I. Sinha, AgI/$CuWO_4$ Z-scheme photocatalyst for the degradation of organic pollutants: experimental and molecular dynamics studies. J. Colloid Interf Sci. **599**, 717–729 (2021). https://doi.org/10.1016/j.jcis.2021.04.120

14. A.H. Bashal, M. Khalafalla, T.A. Abdel-Basset, Dielectric Properties and AC Conductivity of Chitosan-La_2O_3 Nanocomposite. Arab. J. Sci. Eng. **46**, 5859–5864 (2020). https://doi.org/10.1007/s13369-020-04958-w

15. V. Bertolino, G. Cavallaro, S. Milioto, G. Lazzara, Polysaccharides/Halloysite nanotubes for smart bionanocomposite materials. Carbohydr. Polym. **245**, 116502 (2020). https://doi.org/10.1016/j.carbpol.2020.116502

16. G. Cavallaro, S. Micciulla, L. Chiappisi, G. Lazzara, Chitosan-based smart hybrid materials: a physico-chemical perspective. J. Mater. Chem. B **9**(3), 594–611 (2021). https://doi.org/10.1039/D0TB01865A

17. R.B. Suneetha, P. Selvi, C. Vedhi, Synthesis, structural and electrochemical characterization of Zn doped iron oxide/grapheneoxide/chitosan nanocomposite for supercapacitor application. Vacuum. **164**, 396–404 (2019). https://doi.org/10.1016/j.vacuum.2019.03.051

18. M.I.A. Maksoud, M. Bekhit, D.M. El-Sherif, A.R. Sofy, M.R. Sofy, "Gamma radiation-induced synthesis of a novel chitosan/silver/Mn-Mg ferrite nanocomposite and its impact on cadmium accumulation and translocation in brassica plant growth." Int. J. Biol. Macromol. **194**, 306–316 (2022). https://doi.org/10.1016/j.ijbiomac.2021.11.197

19. A. Sionkowska, M. Wisniewski, J. Skopinska, S. Vicini, E. Marsano, The influence of UV irradiation on the mechanical properties of chitosan/poly(vinyl pyrrolidone) blends. Polym. Degrad. Stab. **88**, 261–267 (2005). https://doi.org/10.1016/j.polymdegradstab.2004.08.018

20. A.M. Abdelghany, M.S. Meikhail, A.H. Oraby, M.A. Aboelwafa, Experimental and DFT studies on the structural and optical properties of chitosan/polyvinyl pyrrolidone/ZnS nanocomposites. Polym. Bull., (2023) in press. DOI:https://doi.org/10.1007/s00289-023-04700-0

21. A.N. Anyakora, O.K. Abubakre, E. Mudiare, M.A.T. Suleiman, Effect of fibre loading and treatment on porosity and water absorption correlated with tensile behaviour of oil palm empty fruit bunch fibre reinforced composites. Adv. Mater. Res. **6**(4), 329 (2017). https://doi.org/10.12989/amr.2017.6.4.329

22. S.A. Baskakov, Y.V. Baskakova, E.V. Dvoretskaya, S.S. Krasnikova, V.A. Lesnichaya, Y.M. Shulga, G.L. Gutsev, Mechanical and water absorption Properties of Waterborne Polyurethane/Graphene oxide composites. Materials. **16**(1), 178 (2022). https://doi.org/10.3390/ma16010178

23. A. Paydayesh, L. Heleil, A.S. Dadkhah, Preparation and application of poly (hydroxyl ethyl methacrylate) nanocomposite hydrogels containing iron oxide nanoparticles as wound dressing. Polym. Polym. Compos. **30**, 1–10 (2022). https://doi.org/10.1177/09673911211063106

24. V.R. Pereira, A.M. Isloor, U.K. Bhat, I.A.F. smail, A. Obaid, H.K. Fun, Preparation and performance studies of polysulfone-sulfated nano-titania (S-TiO_2) nanofiltration membranes for dye removal. RSC Adv. **5**(66), 53874–53885 (2015). https://doi.org/10.1039/C5RA07994B

25. P.K. Panda, J.M. Yang, Y.H. Chang, Water-induced shape memory behavior of poly (vinyl alcohol) and p-coumaric acid-modified water-soluble chitosan blended membrane. Carbohydr. Polym. **257**, 117633 (2021). https://doi.org/10.1016/j.carbpol.2021.117633

26. A. Karul, K.T. Tan, C.C. White, D.L. Hunston, S.T. Marshall, B. Akgun, S.K. Satija, C.L. Soles, B.D. Vogt, Impact of polymer modulus/chain mobility on water accumulation at polymer/metal oxide interfaces. Polymer. **50**(14), 3234–3239 (2009). https://doi.org/10.1016/j.polymer.2009.04.064

27. H. Halakoei, M. Ghalkhani, A. Sobhani-Nasab, M. Rahimi-Nasrabadi, An efficient electrochemical sensor based on $CeVO_4$-$CuWO_4$ nanocomposite for methyldopa. Mater. Res. Express. **8**, 085001 (2021). https://doi.org/10.1088/2053-1591/ac16f1

28. G. Mohammed, S. El-Gamal, A.M. El Sayed, S. Saber, Synthesis, structural, optical and electrical characterization of Y_2O_3/poly(ethylene glycol)–poly(vinyl chloride) based nanocomposite solid polymer electrolytes. Polym. Int. **72**, 342–355 (2023). https://doi.org/10.1002/pi.6472

29. S. Sakkara, D. Nataraj, K. Venkatesh, N. Reddy, Influence of Alkali Treatment on the Physicochemical and Mechanical Properties of Starch Chitosan Films. Starch. **71**, 1800084 (2019). https://doi.org/10.1002/star.201800084

30. G.B. Patel, N.L. Singh, F. Singh, Modification of chitosan-based biod egradable polymer by irradiation with MeV ions for electrolyte applications. Mater. Sci. Eng. B **225**, 150–159 (2017). https://doi.org/10.1016/j.mseb.2017.08.023

31. S. Wang, L. Shen, W. Zhang, Y. Tong, Preparation and Mechanical Properties of Chitosan/Carbon Nanotubes Composites. Biomacromolecules. **6**, 3067–3072 (2005). https://doi.org/10.1021/bm050378v

32. E.S. Costa-Júnior, E.F. Barbosa-Stancioli, A.A.P. Mansur, W.L. Vasconcelos, H.S. Mansur, Preparation and characterization of chitosan/poly(vinyl alcohol) chemically crosslinked blends for biomedical applications. Carbohydr.

33. B. Kavitha, R. Karthiga, Synthesis and characterization of $CuWO_4$ as nano-adsorbent for removal of Nile blue and its antimicrobial studies. J. Mater. Environ. Sci. **11**(1), 57–68 (2020)

34. H. Dweik, W. Sultan, M. Sowwan, S. Makharza, Analysis characterization and some Properties of Polyacrylamide Copper Complexes. "Int J. Polym. Mater. Po. **57**(3), 228–244 (2008). https://doi.org/10.1080/00914030701413280

35. H. Mittal, A.A. Alili, P.P. Morajkar, S.M. Alhassan, GO crosslinked hydrogel nanocomposites of chitosan/carboxymethyl cellulose – A versatile adsorbent for the treatment of dyes contaminated wastewater. Int. J. Biolog Macromolec. **167**, 1248–1261 (2021). https://doi.org/10.1016/j.ijbiomac.2020.11.079

36. J. Ahmed, M. Mulla, Y.A. Arfat, L.A. Thai, Mechanical, thermal, structural and barrier properties of crab shell chitosan/graphene oxide composite films. Food Hydrocolloid. **71**, 141–148 (2017). https://doi.org/10.1016/j.foodhyd.2017.05.013

37. G. Mohammed, A.M. El Sayed, W.M. Morsi, Spectroscopic, thermal, and electrical properties of MgO/ polyvinylpyrrolidone/ polyvinyl alcohol nanocomposites. J. Phys. Chem. Solids. **115**, 238–247 (2018). https://doi.org/10.1016/j.jpcs.2017.12.050

38. C. Song, H. Yu, M. Zhang, Y. Yang, G. Zhang, Physicochemical properties and antioxidant activity of chitosan from the blowfly Chrysomya megacephala larvae. Int. J. Biolog Macromol. **60**, 347–354 (2013). https://doi.org/10.1016/j.ijbiomac.2013.05.039

39. A.M. El Sayed, G. Khabiri, Spectroscopic, Optical and Dielectric Investigation of (mg, Cu, Ni, or cd) acetates' influence on Carboxymethyl Cellulose Sodium Salt/Polyvinylpyrrolidone Polymer Electrolyte Films. J. Electron. Mater. **49**(4), 2381–2392 (2020). https://doi.org/10.1007/s11664-020-07953-x

40. M. Morsi, A. Rajeh, A. Menazea, Nanosecond laser-irradiation assisted the improvement of structural, optical and thermal properties of polyvinyl pyrrolidone/carboxymethyl cellulose blend filled with gold nanoparticles. J. Mater. Sci. : Mater. Electron. **30**, 2693–2705 (2019). https://doi.org/10.1007/s10854-018-0545-4

41. T.I. Alanazi, A.M. El, Sayed, Characterization of Mg–Pb–O systems, and MgPbO–thermoplastic blend: nanocomposites for photonic and microelectronic devices. J. Phys. Chem. Solids. **178**, 111346 (2023). https://doi.org/10.1016/j.jpcs.2023.111346

Polym. **76**, 472–481 (2009). https://doi.org/10.1016/j.carbpol.2008.11.015

42. T.-P. Nguyen, Polymer-based nanocomposites for organic optoelectronic devices. A review. Surf. Coat. Technol. **206**, 742–752 (2011). https://doi.org/10.1016/j.surfcoat.2011.07.010

43. A.M. El Sayed, W.M. Morsi, Dielectric relaxation and Optical Properties of polyvinyl Chloride/Lead Monoxide Nanocomposites. Polym. Compos. **34**, 2031–2039 (2013). https://doi.org/10.1002/pc.22611

44. T. Fahmy, H. Elhendawi, W.B. Elsharkawy, F.M. Reicha, AC conductivity and dielectric relaxation of chitosan/poly(vinyl alcohol) biopolymer polyblend. Bull. Mater. Sci. **43**, 243 (2020). https://doi.org/10.1007/s12034-020-02207-2

45. H.I. Elsaeedy, H.E. Ali, H. Algarni, I.S. Yahia, Nonlinear behavior of the current–voltage characteristics for erbium-doped PVA polymeric composite films. Appl. Phys. A **125**, 79 (2019). https://doi.org/10.1007/s00339-018-2375-x

46. D.C. Bharati, P. Rawat, A.L. Saroj, Structural, thermal, and ion dynamics studies of PVA-CS-NaI-based biopolymer electrolyte films. J. Solid State Electrochem. **25**, 1727–1741 (2021). https://doi.org/10.1007/s10008-021-04946-6

47. M.K. Mishra, S. Moharana, B. Behera, R.N. Mahaling, Surface functionalization of $BiFeO_3$: a pathway for the enhancement of dielectric and electrical properties of poly(methyl methacrylate)–$BiFeO_3$ composite films. Front. Mater. Sci. **11**(1), 82–91 (2017). https://doi.org/10.1007/s11706-017-0364-1

48. A.M. El, Sayed, Aspects of structural, optical properties, and relaxation in ($BiFeO_3$ or $NaTiO_3$)–PMMA: hybrid films for dielectric applications. J. Phys. Chem. Solids. **148**, 109767 (2021). https://doi.org/10.1016/j.jpcs.2020.109767